Binary Fe−Co Alloy Nanoparticles Showing Significant Enhancement in Electrocatalytic Activity Compared with Bulk Alloys

Jahangeer Ahmed,[†] Bharat Kumar,[†] Amos M. Mugweru,[‡] Phong Trinh,[‡]
Kandalam V. Ramanujachary,[‡] Samuel E. Lofland,[§] Govind,[||] and Ashok K. Ganguli*,[†]

Department of Chemistry, Indian Institute of Technology, Hauz Khas, New Delhi, 110016, India, Department of Chemistry and Biochemistry, Rowan University, 201 Mullica Hill Road, Glassboro, New Jersey 08028, United States, Department of Physics and Astronomy, Rowan University, 201 Mullica Hill Road, Glassboro, New Jersey 08028, United States, and Surface Physics & Nanostructures, National Physical Laboratory (CSIR), New Delhi, 110012, India

Microemulsion-based synthesis of Fe−Co alloy nanoparticles has been reported for the first time. Spherical, uniform, and highly monodisperse nanoparticles of $Fe_{75}Co_{25}$, $Fe_{67}Co_{33}$, $Fe_{50}Co_{50}$, and $Fe_{33}Co_{67}$ with an average size of 20, 25, 10, and 40 nm, respectively, were synthesized. These nanoparticles crystallize in a body-centered cubic cell. A higher cobalt content led to the formation of biphasic mixtures. Energy-dispersive X-ray spectroscopy studies confirmed the Fe/Co ratios. Nanoparticles of the $Fe_{33}Co_{67}$ alloy show higher hydrogen and oxygen evolution efficiencies (over 100 times) compared with other Fe−Co alloys of nanocrystalline or bulk form. The Fe−Co alloy nanoparticles also show ferromagnetism.

1. Introduction

Fe−Co alloys exhibit a variety of structural,[1−3] mechanical,[4−6] optical,[7] electronic,[7,8] magnetic,[2−4,6−8] and electrocatalytic[9] properties. The crystal structure of the $Fe_{100−x}Co_x$ alloy depends on the temperature and relative ratio of Co and Fe. For $x < 70$ Co, the Fe−Co alloys have a body-centered cubic structure below ∼730 °C and a face-centered cubic structure at higher temperature.[6] Nanosized alloy particles exhibit drastically different properties compared with bulk materials.[10] Fe−Co alloy nanoparticles are ferromagnetic[11] with excellent soft magnetic properties equivalent or superior to those of conventional materials, which are being used in perpendicular magnetic recording media, highly sensitive magnetic sensors, toners, imaging reagents, and magnetic carriers.[5,6,10−13] Nanostructured particles of Fe−Co alloys have earlier been fabricated from chemical[9,15−17] and physical routes.[18−21] Other techniques, such as electrodeposition,[22] mechanical alloying,[1−4,11] sonochemical,[23] polyol processes,[24] decomposition of organometallic precursors,[25] and chemical vapor condensation[26] are also known. Here, we introduce a microemulsion method for obtaining Fe−Co alloy nanoparticles with varying stoichiometries.

The microemulsion method has earlier been employed to obtain a number of metallic (Pt, Pb, Fe, Cd, Ag, Au, Cu, Ni, and Co)[27−30] and bimetallic nanoparticles (Co−Ni, Cu−Ni, Au−Ag, Au−Pd, and Au−Pt).[29,31−34] However, Fe−Co alloy nanoparticles have not been reported so far by the microemulsion method (reverse micelles). Reverse micelles are appropriate reactors for the synthesis of monodisperse nanoparticles with a narrow size distribution.[30] In this paper, we report the synthesis of Fe−Co alloy nanoparticles using the microemulsion method for the first time. We have characterized the alloy nanoparticles using powder X-ray diffraction (PXRD) studies, high-resolution transmission electron microscopy (HRTEM), electron diffraction, and energy-dispersive X-ray spectroscopy (EDS) studies. Magnetic and electrocatalytic properties (both hydrogen and oxygen evolution reaction studies) have been investigated in detail.

2. Experimental Section

$FeCl_3$ (Qualigens, 96%), $(CH_3COO)_2Co \cdot 4H_2O$ (CDH, 99%), $NaBH_4$ (Spectrochem, 98%), cetyl trimethylammonium bromide (CTAB) (Spectrochem, AR, 99%), 1-butanol (Qualigens, 99.5%), and isooctane (Spectrochem, 99%) were used in the synthesis of the Fe−Co alloy nanoparticles. CTAB was the surfactant, 1-butanol the cosurfactant, and isooctane the oil phase. Three microemulsions with different aqueous phases containing 0.1 M $FeCl_3 \cdot 3H_2O$, 0.1 M cobalt acetate, and 1.0 M $NaBH_4$ were prepared. The weight fractions of various constituents in these microemulsions were as follows: 16.76% CTAB, 13.90% 1-butanol, 59.29% isooctane, and the remaining 10.05% aqueous phase. These microemulsions were mixed slowly on a magnetic stirrer, and a brown-colored precipitate was obtained. The precipitate (precursor) was washed with a 1:1 chloroform/ methanol mixture and dried in air. The above precursor, when annealed in a hydrogen atmosphere at 700 °C for 6 h, led to the formation of a monophasic bimetallic $x = 50$ alloy. We have also synthesized nanoparticles with $x = 25$, 33, and 67 using the same method as given above by varying the molar ratio (starting with appropriate stoichiometries of Fe and Co solutions). All alloy nanopowders were black in color. At higher cobalt concentrations ($x > 70$), mixed phases were obtained.

PXRD studies were carried out on a Bruker D8 Advance diffractometer with Ni-filtered Co−Kα radiation with a scan speed of 0.5 s and scan step of 0.02°. The cell parameters were determined from a least-squares fitting of all observed reflections with quartz as the external standard. TEM studies were carried out with a Technai G² 20 electron microscope operating at 200 kV. The specimens for TEM were prepared by dispersing the
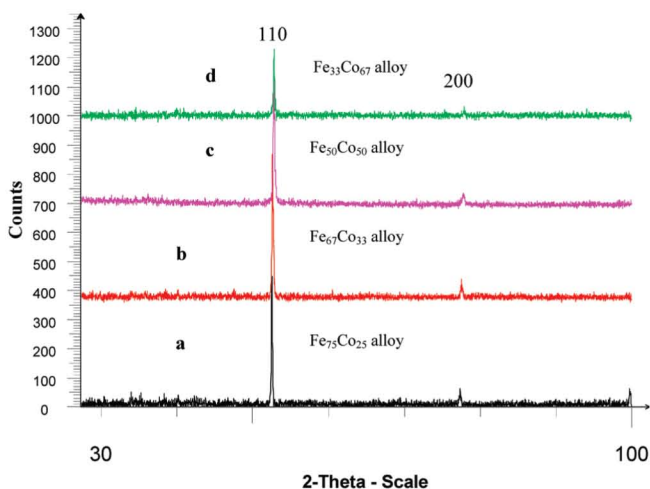
Figure 1. Powder X-ray diffraction patterns of nanocrystalline bimetallic alloys of (a) $Fe_{75}Co_{25}$, (b) $Fe_{67}Co_{33}$, (c) $Fe_{50}Co_{50}$, and (d) $Fe_{33}Co_{67}$.

nanoparticles in acetone by ultrasonic treatment, dropping onto a porous carbon film supported on a copper grid, and then drying in air. X-ray photoelectron spectroscopy was performed in an ultra-high-vacuum chamber (P H1257) with a base pressure of 4×10^{-10} Torr. The XPS spectrometer was equipped with a high-resolution hemispherical electron energy analyzer (279.4 mm diameter) with a resolution of 25 meV and a dual anode Mg/Al Kα X-ray source. An Al (Kα) source with an excitation energy of 1486.6 eV was employed in this study. The general scan showed very small C and O impurities.

Cyclic voltammetry (CV) was carried out with a computer-controlled electrochemical workstation (Autolab 302N/FRA) with the Ohmic drop 98% compensated. The reference electrode was Ag/AgCl while Pt wire was used as the counter electrode (Bioanalytical Systems Inc.). Glassy carbon was used as the working electrode (0.07 cm²), which was first polished with 1 μm diamond polishing paste, then ultrasonicated in distilled water for 1 min before immobilizing the different nanomaterials for either hydrogen or oxygen evolution reactions. A 5 mg portion of Fe–Co alloy nanoparticles was mixed with 2 μL of polyvinylidene fluoride. The mixture was placed on the glassy carbon electrode and air-dried for about 1 h. The glassy carbon electrode was then placed in the cell containing about 5 mL of 0.5 M KOH solution. For each experiment, freshly prepared electrodes and solutions were used. The experiments were carried out at room temperature (22−23 °C). Cyclic voltammetry was carried out at a scan rate of 40 mV/s with a peak window between 0 and −1.5 V versus a Ag/AgCl electrode for the hydrogen evolution reaction and from 0 to 0.8 V versus Ag/AgCl for the oxygen evolution reaction. Amperometry was carried out for 200 s for each electrode with the potential fixed at −1.4 V versus Ag/AgCl for hydrogen evolution and at 0.8 V for the oxygen evolution reaction.

The magnetization studies were carried out at temperatures ranging from 10 to 300 K, in applied fields of up to 10 kOe with a Quantum Design Physical Properties Measurement System.

3. Results and Discussion

Powder X-ray diffraction studies (Figure 1) showed that pure crystalline nanoparticles of varying stoichiometries were synthesized. All the reflections of each pattern could be indexed on the basis of a body-centered cubic (bcc) unit cell. The refined
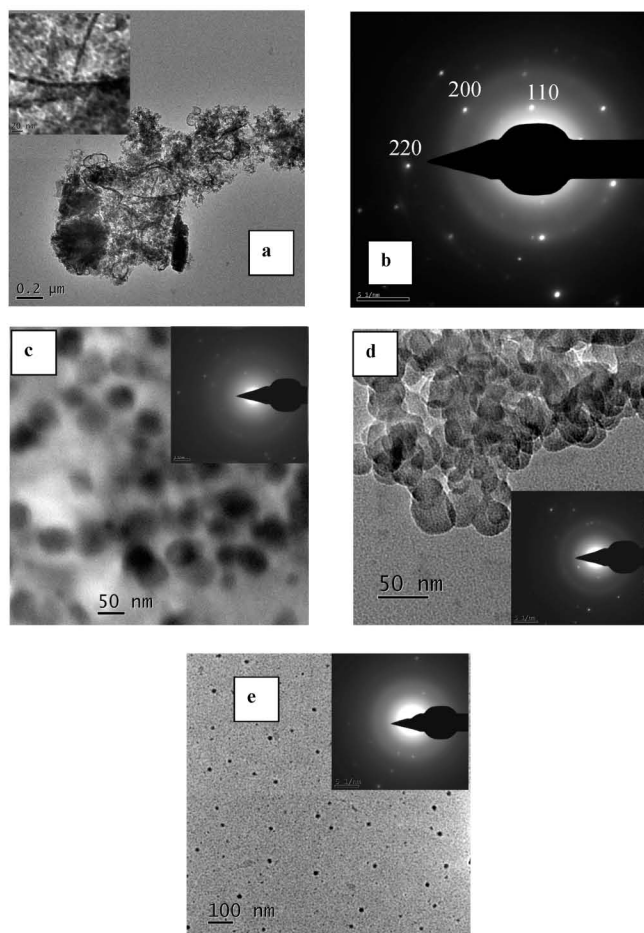

Figure 2. (a) TEM micrographs of $Fe_{50}Co_{50}$. (b) Electron diffraction pattern of $Fe_{50}Co_{50}$ nanoparticles. (c) TEM micrograph of $Fe_{33}Co_{67}$. (d) TEM micrograph of $Fe_{67}Co_{33}$. (e) TEM micrograph of $Fe_{75}Co_{25}$ alloy nanoparticles. The insets of panels (a)−(e) show the high-magnification TEM image of $Fe_{50}Co_{50}$ and electron diffraction patterns of $Fe_{33}Co_{67}$, $Fe_{67}Co_{33}$, and $Fe_{75}Co_{25}$ alloy nanoparticles, respectively.

lattice parameters of the nanoparticles were found to be 2.8450(1), 2.8481(9), 2.8567(3), and 2.8620(1) Å for $Fe_{75}Co_{25}$, $Fe_{67}Co_{33}$, $Fe_{50}Co_{50}$, and $Fe_{33}Co_{67}$, respectively, which is similar to the lattice parameters reported earlier.[15] The increase in lattice parameter with x is in accordance with the larger size of Co. Note that the lattice parameter of bcc iron is 2.840 Å, whereas that of fcc cobalt is 3.560 Å. A mixed phase of Co and Fe−Co alloy nanoparticles was obtained when the composition was loaded in the ratio of 1:3 of Fe/Co systems. Note that Co forms a solid solution with Fe when x < 70.[14]

Figure 2 shows the TEM micrographs of Fe−Co nanoparticles. The microscopic studies showed the formation of $Fe_{50}Co_{50}$ alloy nanowires (Figure 2a). On closer inspection (shown by a HRTEM image), these nanowires appeared to be assembled from spherical nanoparticles (inset of Figure 2a). The average size of these spherical nanoparticles was found to be ∼10 nm. Self-assembly of $Fe_{50}Co_{50}$ nanoparticles may be due to their magnetic interaction. Electron diffraction patterns showed the formation of pure bcc $Fe_{50}Co_{50}$ nanoparticles (Figure 2b). TEM micrographs of $Fe_{33}Co_{67}$, $Fe_{67}Co_{33}$, and $Fe_{75}Co_{25}$ showed highly uniform and monodisperse spherical-shaped nanoparticles with the average sizes of 40, 25, and 20 nm, respectively (Figure 2c−e), and the corresponding electron diffraction patterns (insets, Figure 2c−e, respectively) clearly indicated the presence of only a bcc structure, the low-temperature bulk phase.[6] EDS (Figure 3) confirmed the compositions of the nanoparticles to
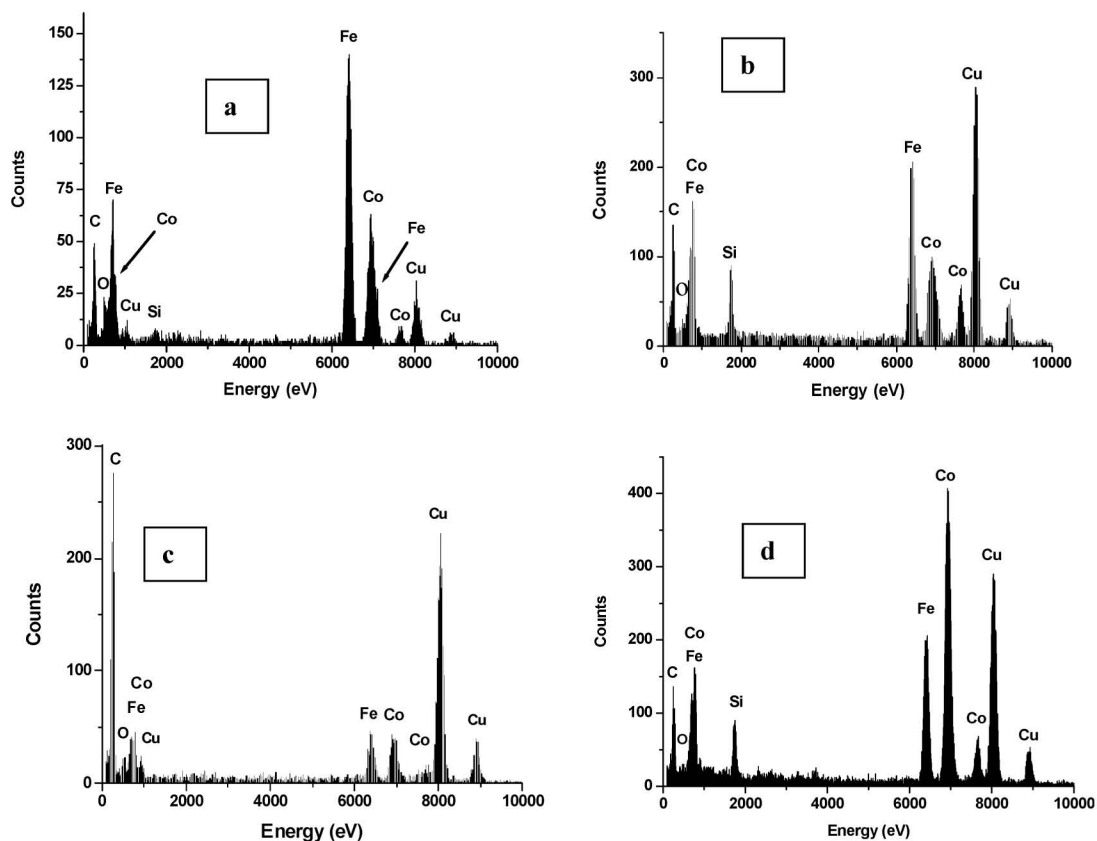
Figure 3. EDAX analysis of (a) $Fe_{75}Co_{25}$, (b) $Fe_{67}Co_{33}$, (c) $Fe_{50}Co_{50}$, and (d) $Fe_{33}Co_{67}$ alloy nanoparticles.

be $Fe_{72}Co_{28}$, $Fe_{67}Co_{33}$, $Fe_{52}Co_{48}$, and $Fe_{38}Co_{62}$ (Figure 3a−d), in accord with the initial loaded stoichiometries ($Fe_{75}Co_{25}$, $Fe_{67}Co_{33}$, $Fe_{50}Co_{50}$, and $Fe_{33}Co_{67}$, respectively). The EDS studies suggested that the surface of these nanoparticles was oxidized to a small extent.

Figure 4 shows the XPS spectra of Fe−Co alloy nanoparticles where core level spectra of Fe 2p and Co 2p versus binding energy are presented. Figure 4a shows the photoemission peak with Fe $2p_{3/2}$ at a binding energy of 706.8 eV,[35] which indicates the presence of elemental iron, Fe(0). A little bump is observed at 709.8 eV, due to Fe^{2+},[36] suggesting slight oxidation of Fe on the surface of the sample. A photoemission peak of Co $2p_{3/2}$ is shown at 778.2 eV (Figure 4b), which indicates the presence of pure Co metal.[35] However, there is also a shoulder at about 781 eV corresponding to the Co^{2+} oxidation state,[35] evidence of a minor surface oxidation of Co as well.

From the depth profile curve obtained from XPS studies, we can observe the variation of Fe and Co XPS signals by removal of the surface layers of the nanoparticles by 4 keV Ar^+ ion bombardment. The percentage composition of Fe and Co in Fe−Co nanoparticles with Ar^+ ion depth profiling is shown in Figure 5. Knowing that the average particle size is about 10 nm (for the $Fe_{50}Co_{50}$ nanoparticles) from the TEM data, we calibrate the ion dose in terms of particle size along the beam axis. The composition (relative %) of each metal is calculated from the corresponding atomic scattering factors. Using geometrical consideration and ignoring preferential sputtering and the inelastic mean free path of the core electrons, we quantitatively estimate the composition by assuming a radial dependence of the density of each element.[31] From the above studies, we observe that the average stoichiometry of the nanoparticle was found to be 1:1 for the $Fe_{50}Co_{50}$ alloy nanoparticles (Figure 5) as expected. The compositions of $Fe_{75}Co_{25}$, $Fe_{67}Co_{33}$, and

$Fe_{33}Co_{67}$ alloy nanoparticles are also in accordance with the initial loaded stoichiometry.

Electrochemical characterization of these nanoparticles was studied using cyclic voltammetry and amperometry. Figure 6 shows cyclic voltammograms of various alloy nanoparticles with different compositions. The electrode containing $Fe_{33}Co_{67}$ nanoparticles showed an increased oxidation current at around 0.57 V, whereas the oxidation current for $Fe_{67}Co_{33}$ and $Fe_{75}Co_{25}$ alloy nanoparticles occurred at about 0.75 V versus a Ag/AgCl reference electrode. The current increase at these potentials is due to the following reaction at the electrode surface.

$$4OH^- \rightarrow 2H_2O + O_2 + 4e^-$$

At the electrode surface, $Fe_{33}Co_{67}$ nanoparticles generated more current and at a lower potential than both $Fe_{67}Co_{33}$ and $Fe_{75}Co_{25}$ alloy nanoparticles. The peak current is proportional to the amount of oxygen generated during the chemical reaction. The peak current generated using $Fe_{75}Co_{25}$ nanoparticles was much higher than for $Fe_{67}Co_{25}$ alloy nanoparticles at 0.75 V. The currents obtained are a function of both the surface area and the composition of the bimetallic alloy nanoparticles.

Figure 7 shows the chronoamperometric experiments of three electrodes with various alloy nanoparticles of different compositions. Again, the $Fe_{33}Co_{67}$ alloy nanoparticles showed a much larger current than both the $Fe_{67}Co_{33}$ and the $Fe_{75}Co_{25}$ nanoparticles. Less energy is required for OER at the electrode with $Fe_{33}Co_{67}$ alloy nanoparticles than with the electrode containing $Fe_{67}Co_{33}$ or $Fe_{75}Co_{25}$ nanoparticles. Less energy is also required to generate oxygen from the electrode with $Fe_{67}Co_{33}$ than $Fe_{75}Co_{25}$ alloy nanoparticles. For the oxygen evolution reaction,
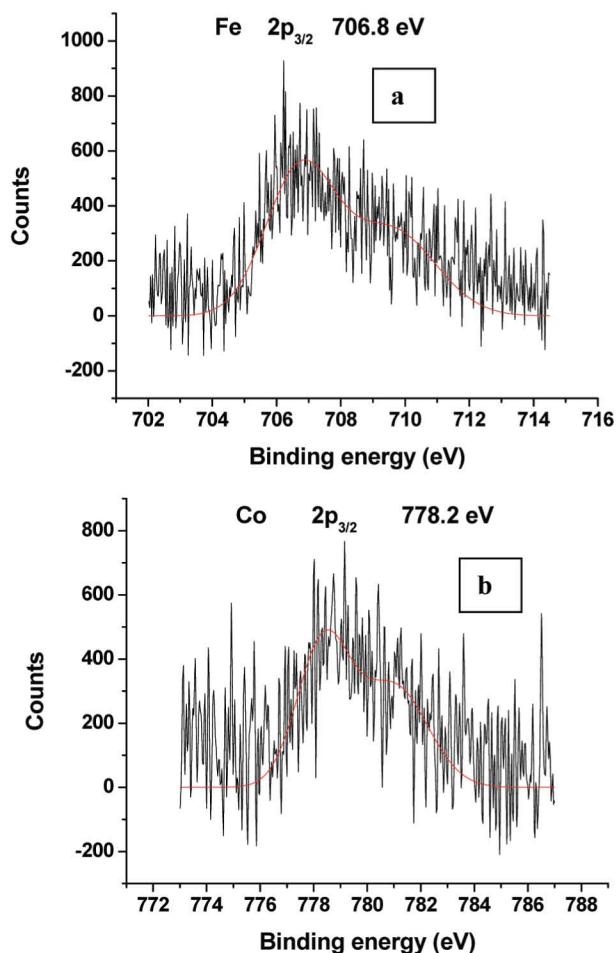
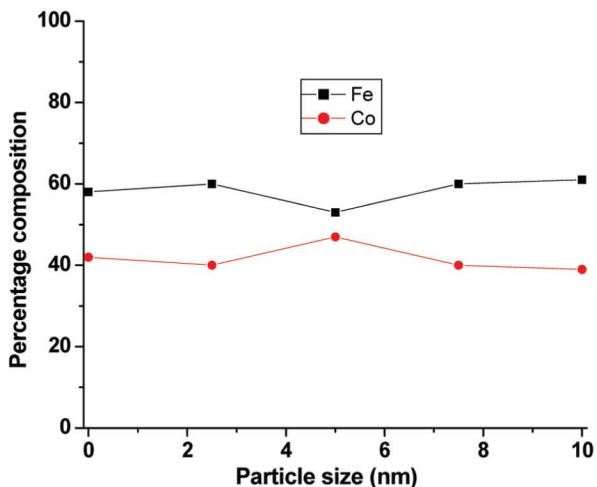**Figure 4.** XPS spectra of Fe−Co alloy nanoparticles in binding energy of (a) Fe 2p and (b) Co 2p.

Figure 5. Depth profile curve obtained from X-ray photoelectron spectroscopy of $Fe_{50}Co_{50}$ alloy nanoparticles.

the $Fe_{33}Co_{67}$ alloy nanoparticles would be the best choice as the evolution reaction occurs at the lowest potential.

The nanoparticles were also evaluated for the hydrogen evolution reaction by applying a negative potential on the electrodes containing the nanoparticles. Figure 8 shows the cyclic voltammograms of various alloy nanoparticles of different compositions scanned from 0 to −1.4 V versus a Ag/AgCl electrode. Two redox peaks were observed for each of the three alloys, which occurred at different potentials. For $Fe_{33}Co_{67}$ nanoparticles, the peaks were around −0.4 and −1.0 V, whereas
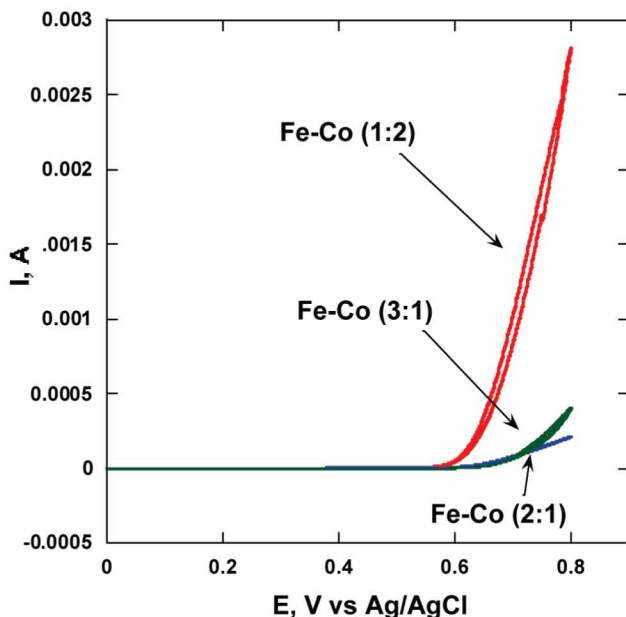

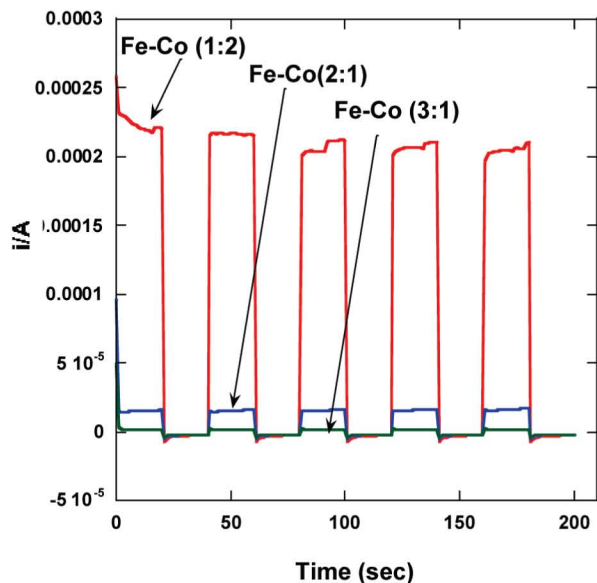**Figure 6.** Cyclic voltammograms of Fe−Co alloy nanoparticles on a glassy carbon electrode in 0.1 M KOH.

Figure 7. Chronoamperometric voltammograms of Fe−Co alloy nanoparticles on a glassy carbon electrode and at 0.8 V vs a Ag/AgCl electrode.

for $Fe_{67}Co_{33}$, the redox potential occurred at about −0.4 and −0.9 V versus a Ag/AgCl electrode. For $Fe_{75}Co_{25}$ alloy nanoparticles, redox peaks occurred at about −0.4 and −0.8 V. From the peak currents generated (above −1.4 V), we observe that $Fe_{33}Co_{67}$ alloy nanoparticles would be much better for hydrogen generation than $Fe_{67}Co_{33}$ or $Fe_{75}Co_{25}$ alloy nanoparticles according to the reaction below.

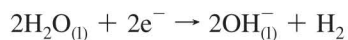$$2H_2O_{(l)} + 2e^- \rightarrow 2OH^-_{(l)} + H_2$$

Figure 9 shows the amperometric voltammograms for these alloy nanoparticles. As observed from cyclic voltammetry, the magnitude of the peak current is as follows: $Fe_{33}Co_{67} > Fe_{67}Co_{33} > Fe_{75}Co_{25}$. All the three alloy nanoparticles showed excellent stability determined from the 10 cycles with each cycle lasting approximately 20 s. The cobalt-rich alloy nanoparticles
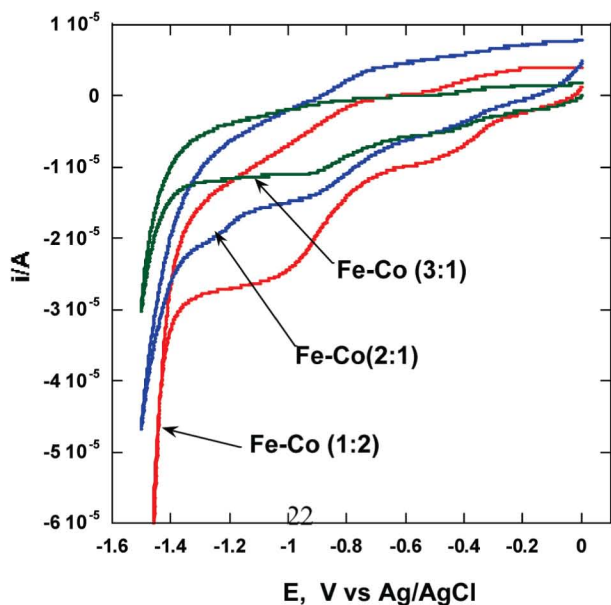
Figure 8. Cyclic voltammograms of Fe−Co alloy nanoparticles on a glassy carbon electrode in 0.1 M KOH scanned at negative potentials.
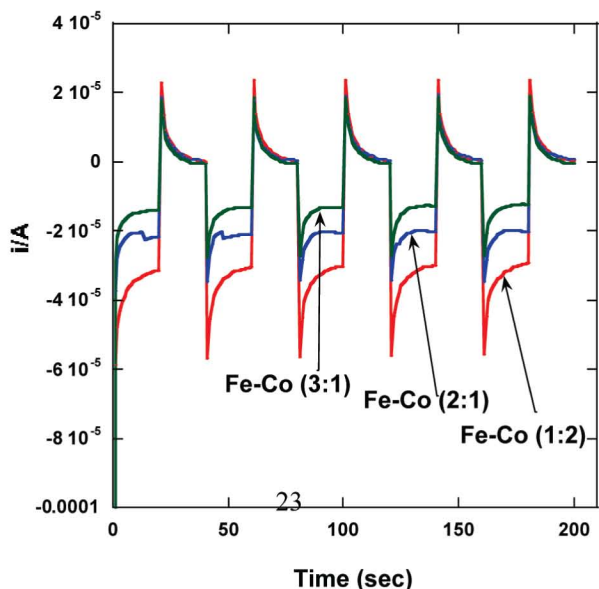

Figure 9. Chronoamperometric voltammograms of Fe−Co alloy nanoparticles on a glassy carbon electrode and at −1.4 V.

($Fe_{33}Co_{67}$) showed superior electrocatalytic behavior compared with amorphous bulk Fe−Co particles.[37] The current density (~40 mA/cm^2) for nanocrystalline $Fe_{33}Co_{67}$ alloy particles was found to be much higher (130 times) than the current generated (~0.3 mA/cm^2) for amorphous bulk Fe−Co alloy powder.[37] Thus, nanosized particles of the Fe−Co alloy would be a better choice as hydrogen and oxygen evolution electrocatalysts compared with bulk alloys. The electrocatalytic activity of alloys with respect to the hydrogen and oxygen evolution reactions (HER and OER) is critically dependent on the surface morphology and composition of the alloy.[38] In the present study, we have investigated the effect of composition of alloy nanoparticles on electrocatalytic behavior (for HER and OER). Note that cobalt is a better electrode material than iron for use in HER and OER.[39−41] Hence, cobalt-rich Fe−Co alloy nanoparticles show superior electrocatalytic behavior.

The field dependence of magnetization of Fe−Co alloy nanoparticles has been investigated from 10 to 300 K. The room-
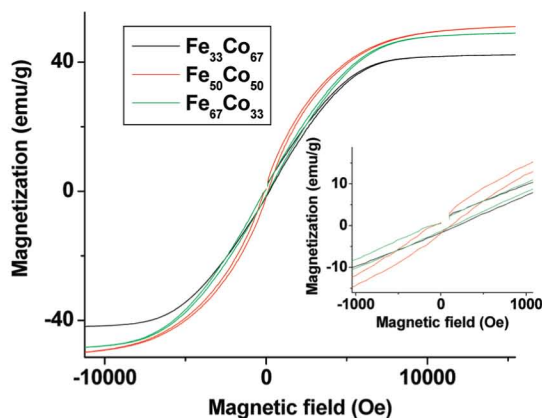

Figure 10. *M* vs *H* plots of Fe−Co alloy nanoparticles at 300 K.

temperature hysteresis loops showed ferromagnetic behavior of Fe−Co nanoparticles, and the saturation magnetization values (M_s) at 300 K are calculated to be 50, 52, and 43 emu/g for nanoparticles with $x = 67$, 50, and 33, respectively (Figure 10). Similar magnetic behavior was also observed at 10 K. The M_s values of Fe−Co nanoparticles are smaller than that reported for the corresponding bulk FeCo alloy (~225 emu/g).[42] M_s values of 205 and 150 emu/g have been reported for spherical particles with an average size of 45 and 40 nm (at 300 K), whereas a value of M_s of 212 emu/g was earlier reported for cube-shaped nanoparticles (~70 nm).[15,23,43] One possibility is that the particles oxidized during the prolonged time between synthesis and measurement. Such oxides are ferri- or antiferromagnetic, leading to a decrease in measured magnetization. Although only minor oxygen was detected by XPS and EDS, both studies were done under ultrahigh vacuum and not long after synthesis.

4. Conclusions

We have used a microemulsion method for the synthesis of $Fe_{75}Co_{25}$, $Fe_{67}Co_{33}$, $Fe_{50}Co_{50}$, and $Fe_{33}Co_{67}$ nanoparticles. The diameter of the particles lies in the range of 10−40 nm. Electrocatalytic studies showed that $Fe_{33}Co_{67}$ nanoparticles are much superior hydrogen and oxygen evolution electrocatalysts compared with $Fe_{67}Co_{33}$ and $Fe_{75}Co_{25}$ nanoparticles. Nanocrystalline $Fe_{33}Co_{67}$ alloy particles also showed a much higher current density (~40 mA/cm^2) than the current generated for bulk Fe−Co alloy powder. These nanoparticles are ferromagnetic, although there is indication of oxidation, leading to reduced magnetization.

References and Notes

(1) Moumeni, H.; Alleg, S.; Greneche, J. M. *J. Alloys Compd.* **2005**, *386*, 12.
(2) Sorescu, M.; Grabias, A. *Intermetallics* **2002**, *10*, 317.
(3) Zelenakova, A.; Oleksakova, D.; Degmova, J.; Kovac, J.; Kollar, P.; Kusy, M.; Sovak, P. *J. Magn. Magn. Mater.* **2007**, *316*, 519.

(4) Elkalkouli, R.; Grosbras, M.; Dinhut, J. F. *Nanostruct. Mater.* **1995**, *5*, 733.

(5) George, E. P.; Gubbi, A. N.; Baker, I.; Robertson, L. *Mater. Sci. Eng., A* **2002**, *329*, 331–325.

(6) Sourmail, T. *Prog. Mater. Sci.* **2005**, *50*, 816.

(7) Kim, K. J.; Lee, S. J.; Lynch, D. W. *Solid State Commun.* **2000**, *114*, 457.

(8) Yuan, P. S.; Wu, H. Q.; Xu, H. Y.; Xu, D. M.; Cao, Y. J.; Wei, X. W. *Mater. Chem. Phys.* **2007**, *105*, 391.

(9) Jo, C.; Lee, J.; Jang, Y. *Chem. Mater.* **2005**, *17*, 2667.

(10) Siegel, R. *Nanostruct. Mater.* **1993**, *3*, 1.

(11) Zeng, Q.; Baker, I.; McCreary, V.; Yan, Z. *J. Magn. Magn. Mater.* **2007**, *318*, 28.

(12) Liu, K.; Nagodawithana, K.; Searson, P. C.; Chien, C. L. *Phys. Rev. B* **1995**, *51*, 7381.

(13) Zheng, M.; Menon, L.; Zeng, H.; Liu, Y.; Bandyopadhyay, S.; Kirby, R. D.; Sellmyer, D. J. *Phys. Rev. B* **2000**, *62*, 12282.

(14) Su, X.; Zheng, H.; Yang, Z.; Zhu, Y.; Pan, A. *J. Mater. Sci.* **2003**, *38*, 4581.

(15) Wei, X. W.; Zhu, G. X.; Liu, Y. J.; Ni, Y. H.; Song, Y.; Xu, Z. *Chem. Mater.* **2008**, *20*, 6248.

(16) Wu, H. Q.; Yuan, P. S.; Xu, H. Y.; Xu, D. M.; Geng, B. Y.; Wei, X. W. *J. Mater. Sci.* **2006**, *41*, 6889.

(17) Lee, B. H.; Lee, Y. J.; Min, K. H.; Kim, D. G.; Kim, Y. D. *Mater. Lett.* **2005**, *59*, 3156.

(18) Bai, J.; Xu, Y. H.; Wang, J. P. *IEEE Trans. Magn.* **2007**, *43*, 3340.

(19) Happy; Mohanty, S. R.; Lee, P.; Tan, T. L.; Springham, S. V.; Patran, A.; Ramanujan, R. V.; Rawat, R. S. *Appl. Surf. Sci.* **2006**, *252*, 2806.

(20) Poddar, P.; Wilson, J. L.; Srikanth, H.; Ravi, B. G.; Wachsmuth, J.; Sudarshan, T. S. *Mater. Sci. Eng., B* **2004**, *106*, 95.

(21) Li, X. G.; Takahashi, S.; Watanabe, K.; Kikuchi, Y.; Koishi, M. *Nano Lett.* **2001**, *1*, 475.

(22) Chen, W.; Tang, S.; Lu, M.; Du, Y. *J. Phys.: Condens. Matter* **2003**, *15*, 4623.

(23) Li, Q.; Li, H.; Pol, V. G.; Bruckental, I.; Koltypin, Y.; Calderon-Moreno, J.; Nowik, I.; Gedanken, A. *New J. Chem.* **2003**, *27*, 1194.

(24) Kodama, D.; Shinoda, K.; Sato, K.; Sato, Y.; Jeyadevan, B.; Tohji, K. *J. Magn. Magn. Mater.* **2007**, *310*, 2396.

(25) Chaubey, G. S.; Barcena, C.; Poudyal, N.; Rong, C.; Gao, J.; Sun, S.; Liu, J. P. *J. Am. Chem. Soc.* **2007**, *129*, 7214.

(26) Oh, S. J.; Choi, C. J.; Kwon, S. J.; Jin, S. H.; Kim, B. K.; Park, J. S. *J. Magn. Magn. Mater.* **2004**, *280*, 147.

(27) Capek, I. *Adv. Colloid Interface Sci.* **2004**, *110*, 49.

(28) Stubenrauch, C.; Wielputz, T.; Sottmann, T.; Roychowdhury, C.; DiSalvo, F. J. *Colloids Surf., A* **2008**, *317*, 328.

(29) Ahmed, J.; Sharma, S.; Ramanujachary, K. V.; Lofland, S. E.; Ganguli, A. K. *J. Colloid Interface Sci.* **2009**, *336*, 814.

(30) Ganguli, A. K.; Ganguly, A.; Vaidya, S. *Chem. Soc. Rev.* **2010**, *39*, 474.

(31) Ahmed, J.; Ramanujachary, K. V.; Lofland, S. E.; Furiato, A.; Gupta, G.; Shivaprasad, S. M.; Ganguli, A. K. *Colloids Surf., A* **2008**, *331*, 206.

(32) Chen, D. H.; Chen, C. J. *J. Mater. Chem.* **2002**, *12*, 1557.

(33) Wu, M. L.; Chen, D. H.; Huang, T. C. *Langmuir* **2001**, *17*, 3877.

(34) Wu, M. L.; Chen, D. H.; Huang, T. C. *Chem. Mater.* **2001**, *13*, 599.

(35) Gao, X.; Tan, S. C.; Wee, A. T. S.; Wu, J.; Kong, L.; Yu, X.; Moser, H. O. *J. Electron Spectrosc. Relat. Phenom.* **2006**, *150*, 11.

(36) Guczi, L.; Pászti, Z.; Frey, K.; Beck, A.; Pet, G.; Daroczy, C. S. *Top. Catal.* **2006**, *39*, 137.

(37) Altube, A.; Pierna, A. R. *Electrochim. Acta* **2004**, *49*, 303.

(38) Shafia Hoor, F.; Aravinda, C. L.; Ahmed, M. F.; Mayanna, S. M. *J. Power Sources* **2001**, *103*, 147.

(39) Brossard, L. *Mater. Chem. Phys.* **1991**, *30*, 61.

(40) Rojas, M.; Fan, C. L.; Miao, H. J.; Piron, D. L. *J. Appl. Electrochem.* **1992**, *22*, 1135.

(41) Schmidt, T.; Wendt, H. *Electrochim. Acta* **1994**, *39*, 1163.

(42) Liu, X.; Morisako, A. *J. Appl. Phys.* **2008**, *103*, 07E726.

(43) Nguyen, Q.; Chinnasamy, C. N.; Yoon, S. D.; Sivasubramanian, S.; Sakai, T.; Baraskar, A.; Mukerjee, S.; Vittoria, C.; Harris, V. G. *J. Appl. Phys.* **2008**, *103*, 07D532.